Showcasing research from Prof. Mingxian Liu's laboratory, School of Chemical Science and Engineering, Tongji University, Shanghai, China.

In situ Nafion-nanofilm oriented (002) Zn electrodeposition for long-term zinc-ion batteries

Our study introduces perfluoropolymer (Nafion) into aqueous electrolyte to activate a thermodynamically ultrastable Zn/electrolyte interface. This ultrathin artificial solid electrolyte interface with zincophilic $-SO_3^-$ groups guides the directional Zn^{2+} electrodeposition along the (002) crystal surface even at high current density, yielding a dendrite-free Zn anode for propelling high-performance zinc-ion batteries.

As featured in:

See Mingxian Liu *et al.*, *Chem. Sci.*, 2024, **15**, 4322.

ROYAL SOCIETY OF CHEMISTRY

rsc.li/chemical-science

Registered charity number: 207890

Chemical Science

ROYAL SOCIETY OF CHEMISTRY

EDGE ARTICLE

View Article Online
View Journal | View Issue

Cite this: *Chem. Sci.*, 2024, **15**, 4322

All publication charges for this article have been paid for by the Royal Society of Chemistry

Received 25th December 2023
Accepted 20th February 2024

DOI: 10.1039/d3sc06935d

rsc.li/chemical-science

In situ Nafion-nanofilm oriented (002) Zn electrodeposition for long-term zinc-ion batteries†

Da Zhang,[a] Ziyang Song,[a] Ling Miao,[a] Yaokang Lv,[b] Lihua Gan[a] and Mingxian Liu *[a]

Dendrite growth and parasitic reactions of a Zn metal anode in aqueous media hinder the development of up-and-coming Zn-ion batteries. Optimizing the crystal growth after Zn nucleation is promising to enable stable cyclic performance of the anode, but directly regulating specific crystal plane growth for homogenized Zn electrodeposition remains highly challenging. Herein, a perfluoropolymer (Nafion) is introduced into an aqueous electrolyte to activate a thermodynamically ultrastable Zn/electrolyte interface for long-term Zn-ion batteries. The low adsorption energy (−2.09 eV) of Nafion molecules on Zn metal ensures the *in situ* formation of a Nafion-nanofilm during the first charge process. This ultrathin artificial solid electrolyte interface with zincophilic $-SO_3^-$ groups guides the directional Zn^{2+} electrodeposition along the (002) crystal surface even at high current density, yielding a dendrite-free Zn anode. The synergic Zn/electrolyte interphase electrochemistry contributes an average coulombic efficiency of 99.71% after 4500 cycles for Zn||Cu cells, and Zn||Zn cells achieve an ultralong lifespan of over 7000 h at 5 mA cm^{-2}. Besides, Zn||MnO_2 cells operate well over 3000 cycles. Even at −40 °C, Zn||Zn cells achieve stable Zn^{2+} plating/stripping for 1200 h.

Introduction

Aqueous zinc-ion batteries (ZIBs) have emerged as one of the advanced electrochemical energy storage systems, characterized by their excellent safety, low cost, and high energy and power densities (820 mA h g^{-1} and 5855 mA h cm^{-3}).[1–6] However, the Zn metal anode in ZIBs encounters significant challenges, including the formation of disordered dendrites and grievous interface polarization reactions (Zn anode corrosion and hydrogen evolution), which restrict cycling performance.[7–12] Conspicuously, the low plating/stripping efficiency of the anode at high current densities (≥5 mA cm^{-2}) and in low-concentration Zn salt (1 M and below) significantly hinders the practical application of ZIBs.[13–16] Typically, protecting the Zn anode by organic–inorganic composite coating is an effective strategy, but the slow ion transport caused by the thicker organic hydrophobic layer limits the diffusion of Zn^{2+} at the solid phase interface (SEI), resulting in an increase in the nucleation potential of Zn^{2+} ions. Besides, organic co-solvents disrupt the hydrogen bonding network of the electrolyte and reduce the ionic conductivity of the original electrolyte. Accordingly, it is necessary to achieve deposition induction and rapid diffusion of Zn^{2+} ions.

Profiting from the stable structure and the abundant zincophilic groups, polymers are widely used as electrode protective layers and electrolyte additives to deliver a widened electrochemical window and accelerate the dissociation of Zn salts.[17–22] As a common cation transfer polymer separator, the protons of Nafion are gradually replaced by Zn^{2+} as the cycling proceeds, causing uniform Zn^{2+} transport at the electrode/electrolyte interface. Specifically, Nafion is combined with zeolite through a solution pouring method to construct an organic–inorganic layer, where the zincophilic Nafion benefits the transport of zinc ions and inorganic zeolites with 0.74 nm micropores inhibit the side reactions at the anode/electrolyte interface to prevent dendrite growth.[23] However, such pouring strategy generally yields a micrometer-scale protective layer which is not conducive to the rapid plating/stripping of zinc ions.[24–29] Beyond that, the present Nafion-based layer at the Zn anode often results in uncontrollable Zn nucleation with a (101) and (110)-dominated texture due to high Zn^{2+} concentration polarization, causing deteriorated hydrogen evolution reaction (HER) and loose Zn plating.[30–32] In contrast, the (002) crystal plane is the most stable texture due to its lowest surface nucleation energy, which can homogenize the Zn electrodeposition to suppress the growth of dendrites and HER reactions, achieving long-term ZIBs.[33–35] Therefore, reducing the thickness of the Nafion-based protective layer from the micrometer to nanometer for rapid plating/stripping of zinc ions,

[a]*Shanghai Key Lab of Chemical Assessment and Sustainability, School of Chemical Science and Engineering, Tongji University, Shanghai, 200092, P. R. China. E-mail: liumx@tongji.edu.cn*

[b]*College of Chemical Engineering, Zhejiang University of Technology, Hangzhou 310014, P. R. China*

† Electronic supplementary information (ESI) available. See DOI: https://doi.org/10.1039/d3sc06935d

accompanied by decreasing the surface nucleation energy for achieving stable Zn electrodeposition to inhibit the HER is expected to boost the anode reversibility and long-term ZIBs, yet not reported.

In this work, we introduce perfluoropolymer (Nafion) molecules to construct an anode micro-electric field and activate a thermodynamically ultrastable zinc anode/electrolyte interface for propelling high-performance ZMBs. The spontaneous adsorption of Nafion (NAF) molecules on the Zn anode ensures the *in situ* generation of zincophilic NAF-film, which regulates the directional and dendrite-free deposition of solvated Zn^{2+} ions, significantly improving the plating/stripping efficiency of the Zn anode. Therefore, Zn‖Zn cells using a $Zn(OTF)_2$-NAF ($OTF^- = CF_3SO_3^-$) electrolyte can cycle over 5000 h, and Zn‖Cu cells achieve an average CE of 99.71% after 4500 cycles at 5 mA cm^{-2}. Significantly, Zn‖MnO_2 cells exhibit remarkable cyclic stability over 3000 cycles. Even at −40 °C, the reversible plating/stripping of Zn‖Zn cells can work over 1200 h. This work offers a design avenue of dendrite-free Zn deposition for ultrastable ZMBs.

Results and discussion

First-principles calculations and systemic experiments were performed to study the Zn^{2+} transport mechanisms in $Zn(OTF)_2$-H_2O and $Zn(OTF)_2$-NAF electrolytes.[36–39] For the $Zn(OTF)_2$-H_2O electrolyte interface (Fig. 1a), when the solvated Zn^{2+} ions migrate to the anode/electrolyte interface, the inhomogeneous Zn^{2+} plating and $Zn(OTF)_2$ decomposition result in potential differentiation at the Zn anode, further leading to the fracturing of the SEI and the generation of H_2 (Fig. S1†). In comparison, NAF molecules show a high binding energy with Zn metal (Fig. S2–S4 and Table S1†), which indicates their great predilection to form a NAF-nanofilm on the Zn anode.[40–45] The unique $-SO_3^-$ functional groups in NAF molecules accept Zn^{2+} ion transportation to the anode interface, avoiding excessive plating on the Cu collector. When a smooth NAF-nanofilm is formed at the anode/electrolyte interface (Fig. 1b), the Zn anode exhibits dense Zn^{2+} plating even at high current densities.

The ionic conductivity of Zn^{2+} ions in various electrolytes was analyzed by electrochemical impedance spectroscopy (EIS) using the formula $\sigma = L/RS$ (where L, R, and S are the separator thickness, bulk resistance, and area, respectively). The $Zn(OTF)_2$-NAF electrolyte shows the smallest resistance of 3.7 Ω (Fig. 1c), corresponding to the fastest Zn^{2+} conductivity of 1.22×10^{-2} S cm^{-1} (Table S2†). The cyclic voltammetry (CV) curves of Zn‖Cu cells show the enhancement of Zn ion transport kinetics by the $Zn(OTF)_2$-NAF electrolyte. With the increase of scan rate from 1 to 4 mV s^{-1}, the thicker SEI affects the transfer rate of Zn^{2+} ions, resulting in lower plating/stripping efficiency in the $Zn(OTF)_2$-H_2O electrolyte (Fig. S5†). Compared to the $Zn(OTF)_2$-H_2O electrolyte, the higher amount of Zn^{2+} ions transported in the $Zn(OTF)_2$-NAF electrolyte (0.85 *vs.* 0.33) also demonstrates the rapid transfer and storage of Zn^{2+} ions in the solid/liquid phase interface (Fig. S6†). Of note, there is no significant polarization reaction at the Zn anode demonstrating stable Zn^{2+} plating/stripping. The X-ray diffraction (XRD) patterns of the Cu substrate of Zn‖Cu cells after cycling at 1 mA cm^{-2} in various electrolytes show obviously different Zn^{2+} plating/stripping (Fig. 1d). Fig. 1e demonstrates the geometric models of charge distributions at the Zn/electrolyte interface. Among different Zn/electrolyte interfaces, Zn–NAF interaction and significant charge transfer induce a larger binding energy of $Zn(OTF)_2$, which accelerates the interfacial Zn^{2+} transfer. The Zn deposited through the NAF-nanofilm, unlike the previous Nafion–zeolite protective layer,[46–51] preferentially grows along the (002) crystal surface to form a dense anode after 200 h, due to a lower binding energy of the NAF-nanofilm and zinc metal anode (Fig. 1f).[52] Notably, the charge density of Zn^{2+} ions deposited in the $Zn(OTF)_2$-NAF electrolyte is more uniform compared to that in the $Zn(OTF)_2$-H_2O electrolyte, which is crucial for dense Zn nucleation and a dendrite-free anode (Fig. 1g). Even when the plating/stripping continues for 2000 h, Zn^{2+} ions still preferentially nucleate along the (002) crystal plane (Fig. S7†).

The Zn^{2+} deposition evolution in electrolytes was analyzed by field emission scanning electron microscopy (SEM) and transmission electron microscopy (TEM). For the $Zn(OTF)_2$-H_2O electrolyte (Fig. 1h), a large amount of blocky Zn appeared on the Cu substrate after a plating/stripping of 24 h. As the operating time increases to 200 h, the irregular growth of dendrites on the Zn anode inevitably leads to SEI damage and $Zn(OTF)_2$ consumption (Fig. S8†). In contrast, the deposition morphology in the $Zn(OTF)_2$-NAF electrolyte is smoother (predominantly hexagonal deposition), maintaining a stable (002) crystal growth (Fig. 1i). The interface of directional crystal growth ((002) plane) reduces the formation of dendrites and delays the corrosion rates of Zn anodes (Fig. S9 and S10†). TEM images clearly show the plating of Zn^{2+} in different electrolytes. With a lower current density (1 mA cm^{-2} and 0.5 mA h cm^{-2}), an inhomogeneous SEI was obtained on the Zn anode, about 480 and 570 nm (Fig. 1j). Besides, obvious fluctuations occur at the Zn anode interface at 5 mA cm^{-2} (Fig. S11†), resulting in uneven SEI thickness and disordered Zn deposition. Notably, the NAF-nanofilm (15 nm in thickness) and SEI (100 nm in thickness) can be observed at the interface between the anode and electrolyte (Fig. 1k), which promises high-kinetics Zn^{2+} transfer. Even at 10 mA cm^{-2}, the SEI in the $Zn(OTF)_2$-NAF electrolyte maintains higher crystallinity compared to that in the $Zn(OTF)_2$-H_2O electrolyte (Fig. S12†).

Ab initio molecular dynamics (AIMD) simulations and density functional theory (DFT) calculations were used to explore the solvation structure and coordination potential during the (dis)charging of ZIBs. For 2 M $Zn(OTF)_2$-H_2O electrolyte (Fig. 2a and S13†), the Zn^{2+} solvation structure includes five H_2O molecules and one OTF^- ion. The more solvated the H_2O molecules, the more severe the hydrogen evolution reactions (Fig. S14–16†). Consequently, NAF co-migrated with Zn^{2+} ions to form a NAF-nanofilm on the Zn anode, effectively guiding the stable deposition of Zn^{2+} ions (Fig. 2b). Compared with the $Zn(OTF)_2$-H_2O electrolyte, the solvated structure of the $Zn(OTF)_2$-NAF electrolyte indicates the decreased proportion of H_2O molecules around Zn^{2+} ions in the solvated shell (Fig. 2c and d). According to molecular dynamics simulations,[53] the

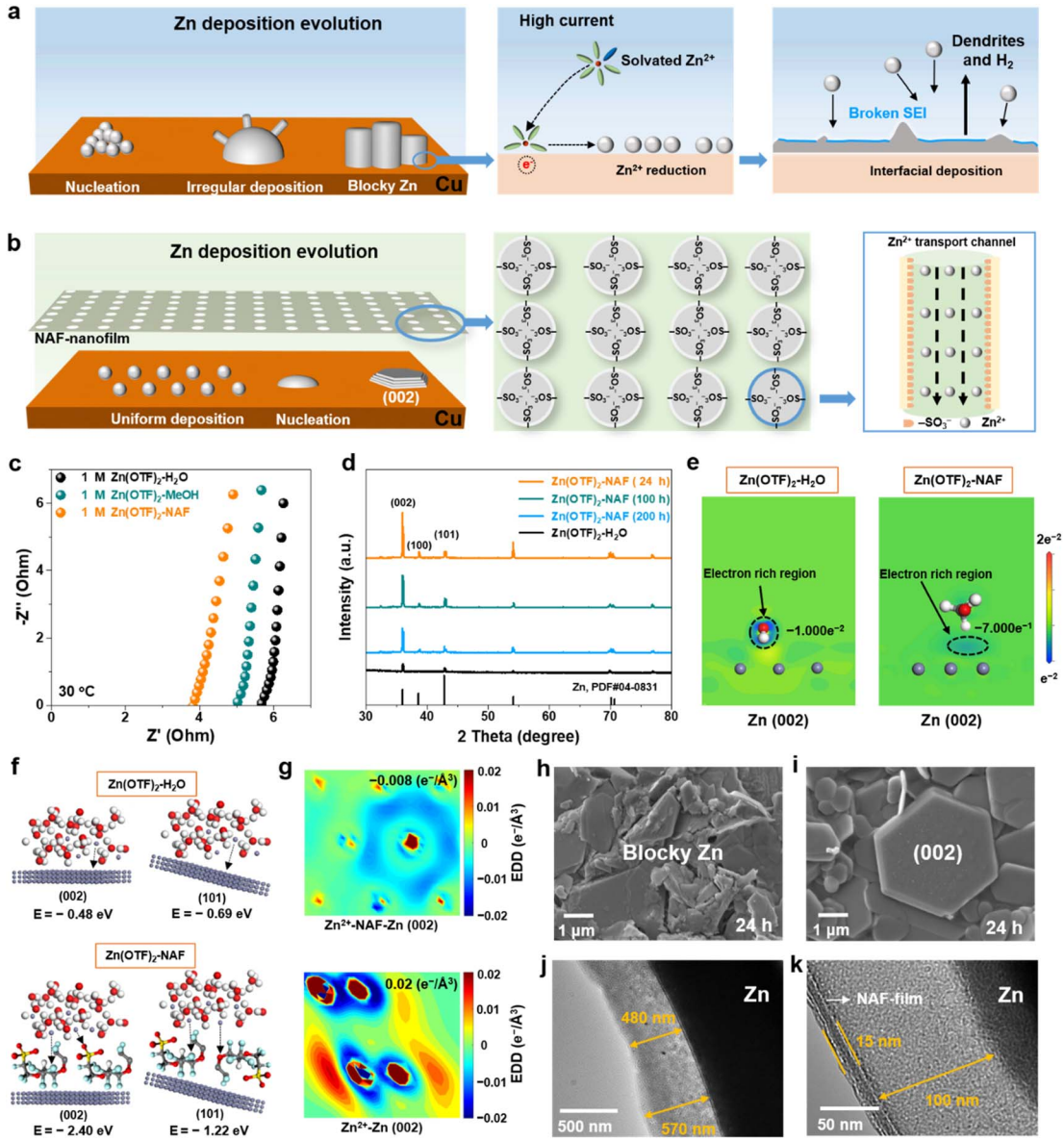

Fig. 1 Schematic diagrams of Zn^{2+} deposition in (a) $Zn(OTF)_2$-H_2O and (b) $Zn(OTF)_2$-NAF electrolytes. (c) Ionic conductivities of various electrolytes. (d) XRD patterns after Zn^{2+} plating/stripping with different electrolytes. (e) Charge distribution at different anode/electrolyte interfaces. (f) Interfacial charge transfer on different crystal planes. (g) The electron density difference of the Zn anode after Zn^{2+} plating on the (002) crystal plane. SEM images of Zn^{2+} plating/stripping evolution after 24 h in (h) $Zn(OTF)_2$-H_2O and (i) $Zn(OTF)_2$-NAF electrolytes. TEM images of SEI thickness at 1 mA cm^{-2} in (j) $Zn(OTF)_2$-H_2O and (k) $Zn(OTF)_2$-NAF electrolytes.

coordination probability of OTF^- with Zn^{2+} in the $Zn(OTF)_2$-NAF electrolyte is significantly higher than that in the $Zn(OTF)_2$-H_2O electrolyte, triggering favorable solvated environments to limit the hydrogen evolution reaction of H_2O molecules, and boosting the Zn^{2+} plating/stripping efficiency at high current densities. The chemical components on the surface of the Zn anode were detected by Ar^+ sputtering X-ray photoelectron spectroscopy (XPS). To maintain the uniformity and integrity of the SEI, all cells were subjected to two constant-current (dis)charging cycles. The elemental contents of the SEI show significant differences for different electrolytes (Fig. S17†). For the $Zn(OTF)_2$-H_2O electrolyte, the inorganic components in the SEI are mainly $ZnCO_3$, ZnO, ZnF_2, and ZnS (Fig. 2e). Notably, ZnF_2 almost disappears with the increase of sputtering time (20 and 40 s), indicating the scarcity of high Zn^{2+} conductivity components in the SEI, and the uneven SEI impedes the rapid transfer and plating/stripping of Zn^{2+}. The detected characteristic peak of OTF^- confirms the continuous decomposition of $Zn(OTF)_2$ during the (dis)charging of ZIBs.[54]

For $Zn(OTF)_2$-MeOH (MeOH = methanol) electrolyte (Fig. S18†), ZnF_2 (684.8 eV) and $*CF_3$ (689.4 eV)[55] can be captured after the etching time reaches 20 s (Table S3†). The results indicate the formation of a ZnF_2 and $ZnCO_3$ polycrystalline phase SEI. However, the solvation structure of Zn^{2+}

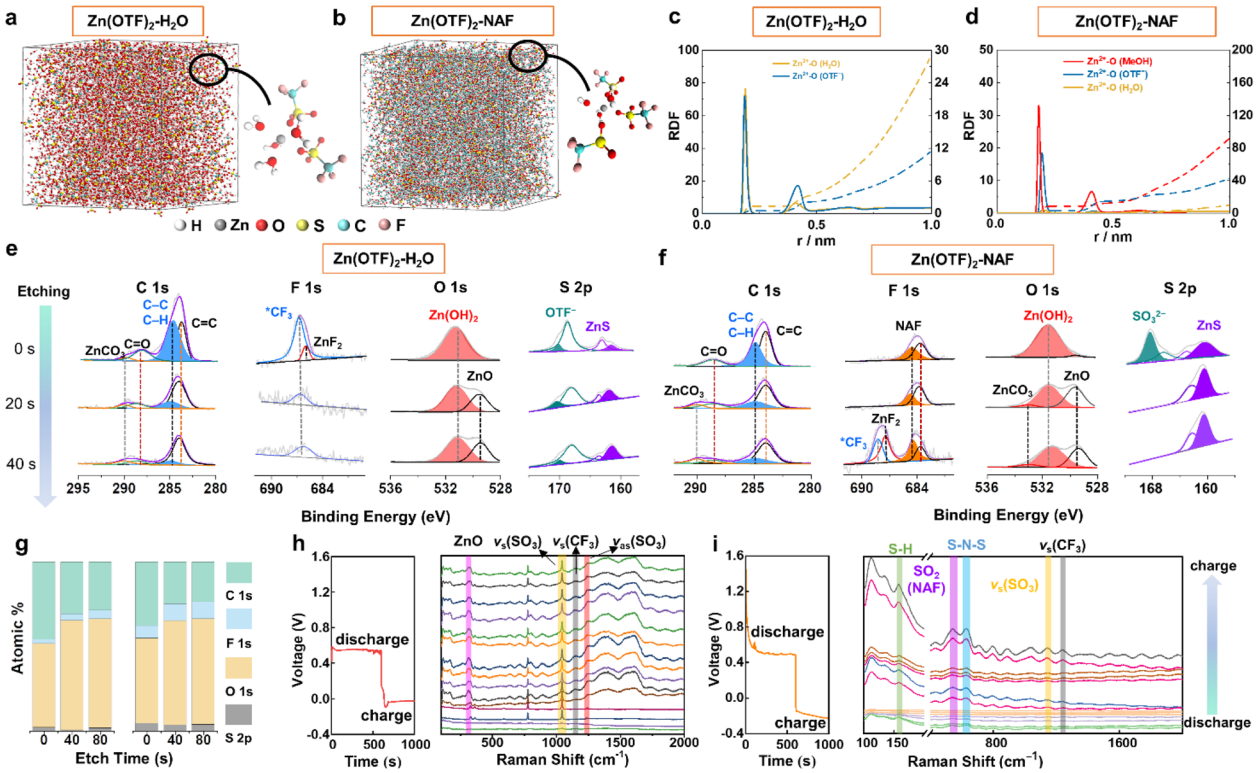

Fig. 2 (a and b) 3D snapshots and corresponding enlarged images of solvation sheaths, and (c and d) radial distribution functions of Zn^{2+}–O in $Zn(OTF)_2$-H_2O and $Zn(OTF)_2$-NAF electrolytes. (e and f) In-depth XPS spectra analysis of different electrolytes. (g) The atomic concentration percentages corresponding to different SEIs. *In situ* Raman test of Zn||Cu cells in (h) $Zn(OTF)_2$-H_2O and (i) $Zn(OTF)_2$-NAF electrolytes.

ions in the $Zn(OTF)_2$-MeOH electrolyte damages the formed SEI and causes sustained consumption of $Zn(OTF)_2$, restricting the long-term cycling performance of ZIBs. Therefore, specific protection needs to be implemented for the Zn anode. Even when the etching time reaches 40 s, the detected ZnF_2 confirms that NAF-SEI has a more complete polycrystalline phase structure (Fig. 2f). As the sputtering time increases, the SO_3^- fraction of NAF is captured on the Zn surface, which verifies the self-adsorption of NAF with Zn.[56] Besides, the protection of the NAF-nanofilm on the Zn anode is confirmed by the disappearance of OTF^- ions. Fig. 2g shows the variation in elemental content of the formed SEI in different electrolytes. The introduction of NAF solution increases the ratio of ZnF_2 and $ZnCO_3$ content in the SEI.

In situ Raman spectroscopy was applied to monitor the Raman peak variations of the Zn anode in the $Zn(OTF)_2$-H_2O electrolyte (Fig. S19†). During discharging (Zn^{2+} migrating to the Cu collector), a significant $Zn(OTF)_2$ component is detected, which is reflected by the peaks at 1036 and 1256 cm^{-1} (Fig. 2h).[57] The characteristic peak of $Zn(OTF)_2$ (1224 cm^{-1})[58] is accurately observed, further confirming the severe hysteresis in the desolvation process of $Zn(OTF)_2$. For the $Zn(OTF)_2$-NAF electrolyte, a noticeable voltage drop at the beginning of the voltage–time curve is attributed to the binding between NAF and Zn (Fig. 2i). Besides, the S–H binding sites of NAF at 156 cm^{-1} are captured.[59] The characteristic peaks of $\nu_s(SO_3)$ and $\nu_{as}(SO_3)$ derived from $Zn(OTF)_2$ can be detected in the $Zn(OTF)_2$-H_2O electrolyte, confirming the precipitation of a large amount of $Zn(OTF)_2$. In contrast, the characteristic peak of $Zn(OTF)_2$ in the $Zn(OTF)_2$-NAF electrolyte is very weak, indicating little $Zn(OTF)_2$ precipitates at the Zn/electrolyte interface and ensuring the long-term stability of ZIBs. The *in situ* attenuated total reflectance-Fourier transform infrared (ATR-FTIR) spectroscopy was utilized to analyse the evolution pattern of the solvation conformation in electrolytes (Fig. 3a). The process of Zn^{2+} plating/stripping was studied under constant-current density (1 mA cm^{-2}) (dis)charging. An obvious OTF^- peak (1032 cm^{-1}) is captured during discharging (Fig. 3b and S20†), indicating that OTF^- molecules remain at the anode/electrolyte interface during Zn^{2+} stripping.

In the voltage–time curves of Zn^{2+} plating/stripping, the cell using the $Zn(OTF)_2$-H_2O electrolyte has a higher overpotential than that using $Zn(OTF)_2$-NAF. A sharp increase in voltage (0.0958 V) is even observed at the end of the charging process (voltage–time curve constant coordinate for 1.7 h, Fig. 3b), which is attributed to the precipitation and decomposition of $Zn(OTF)_2$, leading to an increase in the proportion of H_2O molecules around solvated Zn^{2+} ions, producing more hydrogen gas. Besides, the reversible change of MeOH molecules during (dis)charging indicates the rapid migration of Zn^{2+} ions (Fig. 3c). More importantly, the appearance of the C=O peak suggests a possible bimolecular Cannizzaro disproportionation of MeOH molecules to form methoxy, followed by dehydrogenation to CH_2O^-. The generated CH_2O^- promotes a charge-rich

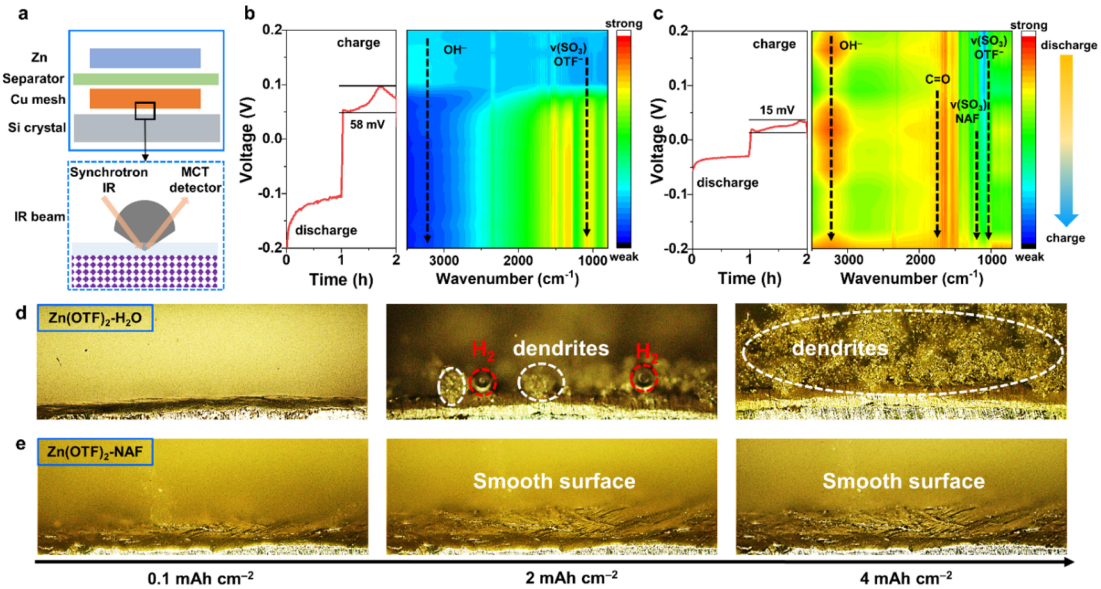

Fig. 3 (a) Schematic diagram of *in situ* ATR-FTIR analysis. (b and c) Voltage–time curves and corresponding ATR-FTIR characterizations in $Zn(OTF)_2$-H_2O and $Zn(OTF)_2$-NAF electrolytes. *In situ* DOF microscope plating images in (d) $Zn(OTF)_2$-H_2O and (e) $Zn(OTF)_2$-NAF electrolytes.

state in the solvation sheath of Zn^{2+} ions and shields it from H_2O molecules, which is crucial for rapid Zn^{2+} transport.[60–62] The dendrite growth and hydrogen production on the Zn anode were directly observed through *in situ* depth of field (DOF) microscopy. For the $Zn(OTF)_2$-H_2O electrolyte, the generation of bubbles can be observed when the Zn^{2+} plating capacity reaches 0.1 mA h cm^{-2} (Fig. 3d). As the discharging process continues, obvious gray-black dendrites appear on the Zn anode, accompanied by severe corrosion after deposition (Fig. S21†). Due to the direct contact between the Zn anode and electrolyte, similar phenomena can also be examined in the $Zn(OTF)_2$-MeOH electrolyte (Fig. S22†). Without the regulation by the NAF-nanofilm, the Zn^{2+} transport kinetics is slower, and the growth of dendrites remains uncontrolled. Compared with the $Zn(OTF)_2$-H_2O electrolyte, the Zn corrosion can be delayed in the $Zn(OTF)_2$-MeOH electrolyte because MeOH significantly reduces the proportion of active H_2O molecules in the solvation sheath of Zn^{2+} ions. No bubbles are observed when the plating capacity reaches 4 mA h cm^{-2}, and the color of the deposited Zn is almost the same as that of the original Zn (Fig. 3e). The *in situ* DOF plating results further indicate the substantially suppressed dendrite growth and H_2 generation in the $Zn(OTF)_2$-NAF electrolyte.

Scanning probe microscopy (SPM) was applied to investigate the plating morphology and interface potential of the Zn anode.[63] Based on the working principle and test results of SPM, the calculation rules of the Zn anode interface potential are obtained:

$$\text{Test 1: } V_{\text{sample}} - V_{\text{tip}} = (\Phi_{\text{tip}} - \Phi_{\text{sample}})/e \quad (1)$$

$$\text{Test 2: } V_{\text{HOPG}} - V_{\text{tip}} = (\Phi_{\text{tip}} - \Phi_{\text{HOPG}})/e \quad (2)$$

$$e(\text{Test 1}) = \Phi_{\text{tip}} - \Phi_{\text{sample}} \quad (3)$$

$$e(\text{Test 2}) = \Phi_{\text{tip}} - \Phi_{\text{HOPG}} \quad (4)$$

Based on formulae (1) and (2), the conversion formulae (3) and (4) between the probe potential and the sample surface potential, and further formula (5) for calculating the surface potential of the sample can be obtained. Φ_{sample} and Φ_{tip} denote the test sample surface potential and probe tip potential, respectively. Φ_{HOPG} is a fixed applied potential of 4.5 eV.

$$\Phi_{\text{sample}} = \Phi_{\text{HOPG}} + e(\text{Test 1} - \text{Test 2}) \quad (5)$$

The height difference of the Zn anode after plating reaches 1.81 and 2.95 μm (plating capacities are 1 and 2 mA h cm^{-2}) in the $Zn(OTF)_2$-H_2O electrolyte (Fig. 4a), together with a minimum local potential value of −2.64 V and a maximum value of 0.93 V through the interfacial potential distribution maps. In contrast, more uniform deposition and potential are achieved in the $Zn(OTF)_2$-NAF electrolyte, as reflected by the height difference of 1.36 μm and the minimum potential value of −0.41 V (Fig. 4b). As a result, the average surface potentials in $Zn(OTF)_2$-H_2O and $Zn(OTF)_2$-NAF electrolytes are determined to be 5.67 and 4.94 eV. The larger average potential on the sample surface indicates the more disordered interfacial charge distribution and irregular Zn^{2+} deposition. The fitted interfacial average potentials in the $Zn(OTF)_2$-H_2O electrolyte are 102.7 and 817.4 mV, which are inferior to those of the $Zn(OTF)_2$-NAF electrolyte (93.3 and 328.1 mV, Fig. 4c and d). The more homogeneous interfacial potential implies a lower activation energy for Zn^{2+} ion migration, thus enabling the dissociation of $Zn(OTF)_2$ at the Zn/NAF interface and accelerating the transport efficiency of Zn^{2+} ions.[64,65] Besides, the Zn^{2+} plating test in the $Zn(OTF)_2$-MeOH electrolyte (Fig. S23†) confirms the attenuated desolvation of Zn^{2+} ions by the NAF-nanofilm. Without the protection of the NAF-nanofilm, the solvation effect remains the

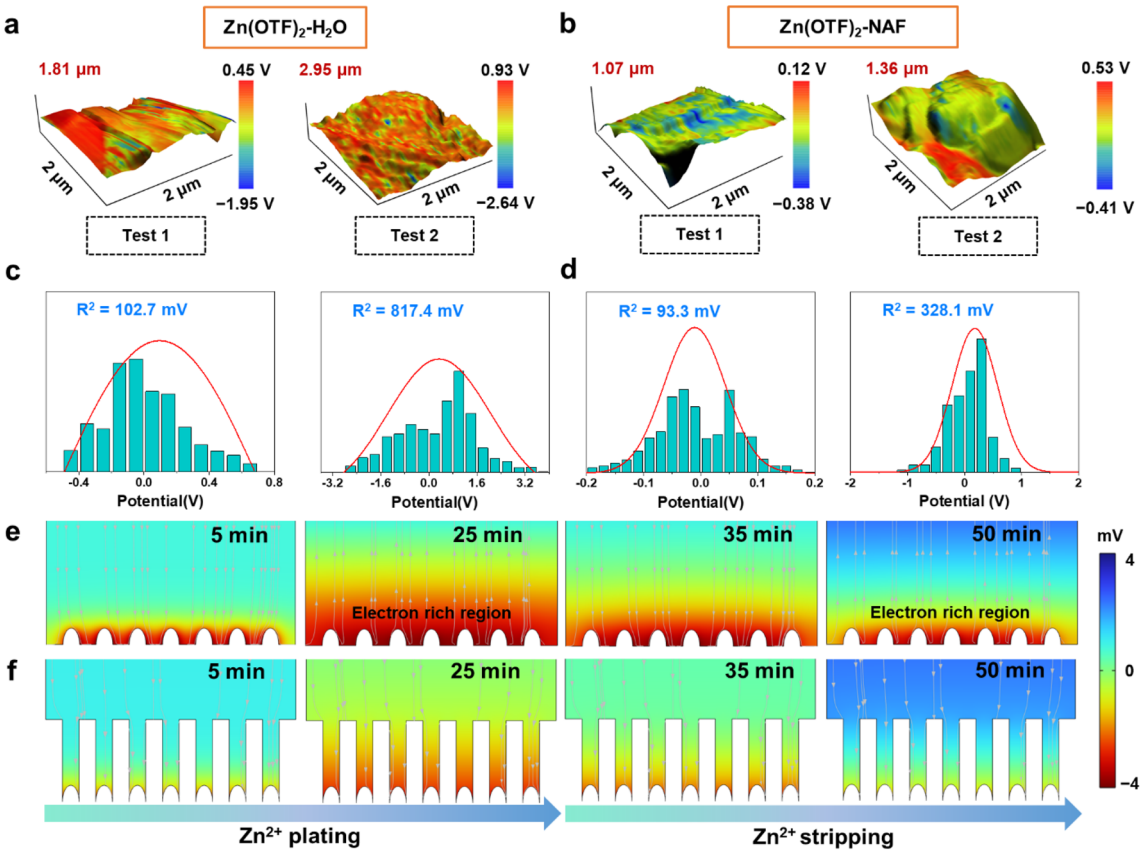

Fig. 4 (a and b) Potential distribution and height variation on the anode surface after Zn^{2+} plating in different electrolytes, tests 1 and 2 were Zn^{2+} plated to 1 and 2 mA h cm^{-2}, respectively (the current density was 0.5 mA cm^{-2}). Gaussian statistical distribution of the interfacial potential in (c) $Zn(OTF)_2$-H_2O and (d) $Zn(OTF)_2$-NAF electrolytes. Simulation of the potential evolution of Zn^{2+} plating/stripping in (e) Zn/electrolyte and (f) Zn-NAF/electrolyte interfaces.

main reason for the slow Zn^{2+} plating/stripping. Based on the deposition potential analysis, the potential simulation of the Zn^{2+} plating/stripping process was performed through the COMSOL potential field.[66] During Zn^{2+} plating (from 5 to 25 min) in $Zn(OTF)_2$-H_2O electrolyte, a local micro-electric field is formed due to the polarization of the electrolyte concentration near the Zn anode (Fig. 4e), which exacerbates the hydrogen evolution reaction (HER) of solvation H_2O molecules and dendrite growth. The potential gradient near the Zn anode remains less than 0 mV during the stripping (35 to 50 min). In the $Zn(OTF)_2$-NAF electrolyte, a microporous film (NAF-nanofilm) is formed on the Zn anode, and the migration of Zn^{2+} is induced by $-SO_3F$ groups on the NAF-nanofilm. The solvation structure fails to reach the Zn anode (Fig. 4f), resulting in a smaller potential gradient compared with the $Zn(OTF)_2$-H_2O electrolyte after 25 min. During Zn^{2+} stripping from the anode interface (35 to 50 min), the potential gradient response of the Zn/NAF/electrolyte interface is faster than that of Zn/electrolyte, which is attributed to the rapid co-migration of dissociated $Zn(OTF)_2$ with the solvated structure. For the $ZnSO_4$-NAF-H_2O electrolyte (Fig. S24–S27†), the micro-electric field constructed by the NAF-nanofilm also enhances the electrochemical performance of ZIBs. The electrochemical properties of Zn||Cu, Zn||Zn, and Zn||MnO_2 cells were systematically studied to verify the facilitation of solvation reconfiguration and Zn^{2+} ion transportation channels in modified electrolytes on Zn^{2+} plating/stripping. According to the voltage–capacity curves of Zn||Cu cells in $Zn(OTF)_2$-H_2O and $Zn(OTF)_2$-NAF electrolytes (Fig. 5a and b), there is no significant difference in the plating/stripping voltage even after 500 cycles. The maximum voltage drop in the $Zn(OTF)_2$-H_2O electrolyte is 0.39 V (20th cycle), which is attributed to the concentration polarization of the interfacial electrolyte and the disordered deposition of Zn^{2+}. Drastic voltage fluctuations lead to the decomposition of $Zn(OTF)_2$ and dendrite growth. The maximum voltage drop in the $Zn(OTF)_2$-NAF electrolyte is only 0.069 V (200th of the cycles), thus ensuring the long-term cycling of ZIBs. The modified Aurbach method was used to analyze the Zn^{2+} desolvation kinetics.[67,68] The NAF-nanofilm significantly improves the Zn^{2+} plating/stripping coulombic efficiency (CE) (Fig. 5c), with the highest value of 99.86%.

Fig. 5d shows the Zn^{2+} plating/stripping CE of Zn||Cu cells using different electrolytes at 5 mA cm^{-2}. An impressive CE of 99.71% is achieved for Zn||Cu cells using the $Zn(OTF)_2$-NAF electrolyte after 4500 cycles. The corresponding charge–discharge curves show more stable voltage fluctuations and gradually decreasing polarization reactions (from the 1st to 4000th cycles), proving the improvement of coulombic

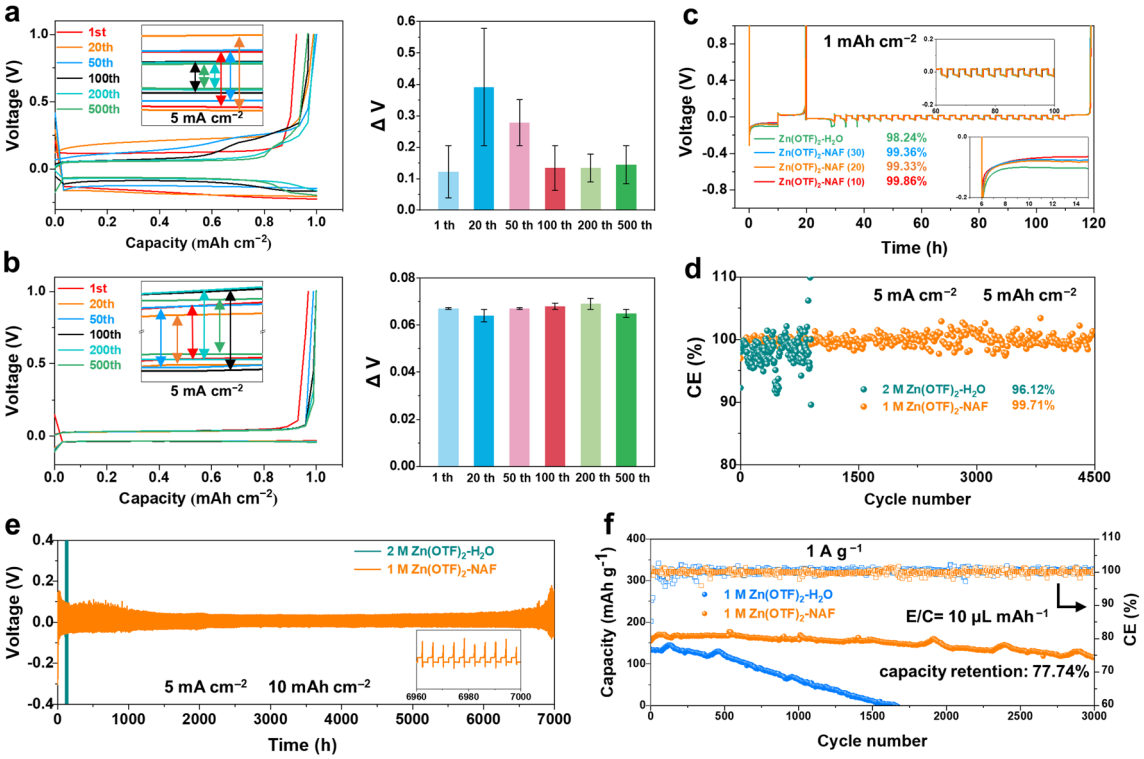

Fig. 5 Long-term deposition voltage–capacity curves and corresponding voltage fluctuation of Zn||Cu cells in (a) $Zn(OTF)_2$-H_2O and (b) $Zn(OTF)_2$-NAF electrolytes. (c) Zn||Cu cells with different electrolytes. (d) The plating/stripping CE of Zn||Cu cells. (e) Long-term performance of Zn||Zn cells. (f) Cycling performance of Zn||MnO_2 cells in different electrolytes at 30 °C.

efficiency in Zn^{2+} ion plating/deposition (Fig. S28†). For comparison, Zn||Cu cells using the $Zn(OTF)_2$-H_2O electrolyte show a CE of 96.12%. Despite the Zn^{2+} plating/stripping in the $Zn(OTF)_2$-MeOH electrolyte reaching 2700 h (while 280 h for the $Zn(OTF)_2$-H_2O electrolyte), the deposition overpotential of Zn^{2+} is continuously increased from 0.3 to 0.65 V. Benefiting from the regulation of Zn^{2+} transportation channels at the Zn anode, the NAF-nanofilm accelerates Zn^{2+} transport in the anode/electrolyte interface. Consequently, Zn||Zn cells using the $Zn(OTF)_2$-NAF electrolyte exhibit remarkable cycling stability with Zn^{2+} plating/stripping for over 7000 h at 5 mA cm^{-2} (Fig. 5e).

Besides, the cell capacity starts to decrease after 100 cycles, corresponding to the gradual depletion of $Zn(OTF)_2$ and the continuous breakage/generation of the SEI (Fig. S29†). In contrast, the Zn||MnO_2 cell using the $Zn(OTF)_2$-NAF electrolyte at 30 °C demonstrates stable 3000 (dis)charging cycles at 1 A g^{-1} with a capacity retention of 77.74% (Fig. 5f). Similar to previous studies,[69] the binding of MeOH to Zn^{2+} ions improves the ionic conductivity of the $Zn(OTF)_2$-NAF electrolyte at low temperatures. Therefore, Zn||Zn cells achieve stable plating/stripping at 1 mA cm^{-2} for 1200 h even at −40 °C (Fig. S30†). Even at −40 °C, Zn||MnO_2 cells using the $Zn(OTF)_2$-NAF electrolyte demonstrate stable 2000 (dis)charging cycles at 0.5 A g^{-1} with a capacity retention of 66.41% (Fig. S31 and S32†). $Zn(OTF)_2$-NAF with excellent electrochemical performance highlights its promising application prospects in advanced ZIBs (Tables S4 and S5†), especially in harsh environments.

Conclusion

In conclusion, Nafion as an additive is introduced into an aqueous electrolyte to construct Zn^{2+} ion directional transmission channels for establishing an ultrastable Zn/electrolyte interface for advanced ZIBs. NAF molecules allow the *in situ* generation of a zincophilic nanofilm which serves as directional Zn^{2+} transport channels with a more negative binding energy to induce Zn^{2+} nucleation along the (002) crystal surface. Benefiting from the artificial ion transportation channels, the dendrite growth and anode corrosion are substantially controlled in $Zn(OTF)_2$-NAF electrolyte. Consequently, Zn||Cu cells achieve an impressive coulombic efficiency of 99.71% after 4500 cycles, and Zn||Zn cells demonstrate stable plating/stripping for 7000 h at 5 mA cm^{-2}. Even at −40 °C, the reversible plating/stripping of Zn||Zn cells can work over 1200 h. This work offers appealing insights into the microscopic Zn/electrolyte interfacial modulation with obviated Zn-dendrites and H_2O-originated parasitic reactions for advanced ZIBs.

Data availability

The data that support the findings of this study are available within the article and its ESI,† or from the corresponding author on reasonable request.

Author contributions

The authors contributed to this work in the following ways: conceptualization (M. Liu, D. Zhang, Z. Song); data curation (D. Zhang); formal analysis (M. Liu, D. Zhang); funding acquisition (M. Liu, L. Gan, Y. Lv); investigation (M. Liu, D. Zhang, L. Miao); methodology (M. Liu, D. Zhang, Z. Song, L. Gan, L. Miao, Y. Lv); project administration (M. Liu); supervision (M. Liu); validation (M. Liu, L. Gan, Y. Lv); visualization (M. Liu, D. Zhang, L. Miao); writing – original draft (D. Zhang); writing – review & editing (M. Liu, D. Zhang, Z. Song).

Conflicts of interest

The authors declare no conflict of interest.

Acknowledgements

This work is financially supported by the National Natural Science Foundation of China (No. 22272118, 22172111, 21905207 and 22309134), the Science and Technology Commission of Shanghai Municipality, China (No. 22ZR1464100, 20ZR1460300 and 19DZ2271500), China Postdoctoral Science Foundation (2022M712402), Shanghai Rising-Star Program (23YF1449200), Zhejiang Provincial Science and Technology Project (2022C01182), and the Fundamental Research Funds for the Central Universities (22120210529 and 2023-3-YB-07).

Notes and references

1 L. Cao, D. Li, T. Pollard, T. Deng, B. Zhang, C. Yang, L. Chen, J. Vatamanu, E. Hu, M. J. Hourwitz, L. Ma, M. Ding, Q. Li, S. Hou, K. Gaskell, J. T. Fourkas, X. Q. Yang, K. Xu, O. Borodin and C. Wang, *Nat. Nanotechnol.*, 2021, **16**, 902–910.
2 Z. Song, L. Miao, H. Duan, L. Ruhlmann, Y. Lv, D. Zhu, L. Li, L. Gan and M. Liu, *Angew. Chem., Int. Ed.*, 2022, **61**, e202208821.
3 N. Yao, X. Chen, Z. H. Fu and Q. Zhang, *Chem. Rev.*, 2022, **122**, 10970–11021.
4 Z. Song, L. Miao, L. Ruhlmann, Y. Lv, L. Li, L. Gan and M. Liu, *Angew. Chem., Int. Ed.*, 2023, **62**, e202219136.
5 Z. Wang, J. Huang, Z. Guo, X. Dong, Y. Liu, Y. Wang and Y. Xia, *Joule*, 2019, **3**, 1289–1300.
6 Z. Song, L. Miao, Y. Lv, L. Gan and M. Liu, *Angew. Chem., Int. Ed.*, 2023, **62**, e202309446.
7 C. Hu, Y. Qin, Z. Song, P. Liu, L. Miao, H. Duan, Y. Lv, L. Xie, M. Liu and L. Gan, *J. Colloid Interface Sci.*, 2024, **658**, 856–864.
8 D. Zhang, R. Gu, Y. Yang, J. Ge, J. Xu, Q. Xu, P. Shi, M. Liu, Z. Guo and Y. Min, *Angew. Chem., Int. Ed.*, 2024, e202315122.
9 Z. Cao, P. Zhuang, X. Zhang, M. Ye, J. Shen and P. M. Ajayan, *Adv. Energy Mater.*, 2020, **10**, 2001599.
10 Y. Pan, S. Liu, K. Sun, X. Chen, B. Wang, K. Wu, X. Cao, W. C. Cheong, R. Shen, A. Han, Z. Chen, L. Zheng, J. Luo, Y. Lin, Y. Liu, D. Wang, Q. Peng, Q. Zhang, C. Chen and Y. Li, *Angew. Chem., Int. Ed.*, 2018, **57**, 8614–8618.
11 C. C. Hou, Y. Wang, L. Zou, M. Wang, H. Liu, Z. Liu, H. F. Wang, C. Li and Q. Xu, *Adv. Mater.*, 2021, **33**, 2101698.
12 L. Miao, Z. Song, W. Du, X. Zheng, Y. Lv, L. Gan and M. Liu, *Mater. Chem. Front.*, 2023, **7**, 2731–2749.
13 P. Xiong, Y. Zhang, J. Zhang, S. H. Baek, L. Zeng, Y. Yao and H. S. Park, *EnergyChem*, 2022, **4**, 100076.
14 H. Dou, M. Xu, B. Wang, Z. Zhang, G. Wen, Y. Zheng, D. Luo, L. Zhao, A. Yu, L. Zhang, Z. Jiang and Z. Chen, *Chem. Soc. Rev.*, 2021, **50**, 986–1029.
15 P. Xiong, C. Lin, Y. Wei, J.-H. Kim, G. Jang, K. Dai, L. Zeng, S. Huang, S. J. Kwon, S. Y. Lee and H. S. Park, *ACS Energy Lett.*, 2023, **8**, 2718–2727.
16 Y. Zhang, Z. Song, L. Miao, Y. Lv, L. Gan and M. Liu, *Angew. Chem., Int. Ed.*, 2024, **63**, e202316835.
17 M. Peng, X. Tang, K. Xiao, T. Hu, K. Yuan and Y. Chen, *Angew. Chem., Int. Ed.*, 2023, **62**, e202302701.
18 B. Niu, Z. Li, D. Luo, X. Ma, Q. Yang, Y. E. Liu, X. Yu, X. He, Y. Qiao and X. Wang, *Energy Environ. Sci.*, 2023, **16**, 1662–1675.
19 Y. Wu, T. Zhang, L. Chen, Z. Zhu, L. Cheng, S. Gu, Z. Li, Z. Tong, H. Li, Y. Li, Z. Lu, W. Zhang and C. S. Lee, *Adv. Energy Mater.*, 2023, **13**, 2300719.
20 Q. Zhang, J. Luan, L. Fu, S. Wu, Y. Tang, X. Ji and H. Wang, *Angew. Chem., Int. Ed.*, 2019, **58**, 15841–15847.
21 P. Xiong, Y. Kang, N. Yao, X. Chen, H. Mao, W.-S. Jang, D. M. Halat, Z. H. Fu, M. H. Jung, H. Y. Jeong, Y. M. Kim, J. A. Reimer, Q. Zhang and H. S. Park, *ACS Energy Lett.*, 2023, **8**, 1613–1625.
22 Y. Wang, Q. Li, H. Hong, S. Yang, R. Zhang, X. Wang, X. Jin, B. Xiong, S. Bai and C. Zhi, *Nat. Commun.*, 2023, **14**, 3890.
23 Y. Cui, Q. Zhao, X. Wu, X. Chen, J. Yang, Y. Wang, R. Qin, S. Ding, Y. Song, J. Wu, K. Yang, Z. Wang, Z. Mei, Z. Song, H. Wu, Z. Jiang, G. Qian, L. Yang and F. Pan, *Angew. Chem., Int. Ed.*, 2020, **59**, 16594–16601.
24 H. Qiu, X. Du, J. Zhao, Y. Wang, J. Ju, Z. Chen, Z. Hu, D. Yan, X. Zhou and G. Cui, *Nat. Commun.*, 2019, **10**, 5374.
25 Q. Zhang, Y. Ma, Y. Lu, Y. Ni, L. Lin, Z. Hao, Z. Yan, Q. Zhao and J. Chen, *J. Am. Chem. Soc.*, 2022, **144**, 18435–18443.
26 Y. Xie, J. Huang, T. Kong, X. Zhou, K. Wu, X. Liu, J. Yi, L. Xing and Y. Xia, *Energy Storage Mater.*, 2023, **56**, 218–226.
27 J. F. Parker, J. S. Ko, D. R. Rolison and J. W. Long, *Joule*, 2018, **2**, 2519–2527.
28 L. Zhang, I. A. Rodríguez Pérez, H. Jiang, C. Zhang, D. P. Leonard, Q. Guo, W. Wang, S. Han, L. Wang and X. Ji, *Adv. Funct. Mater.*, 2019, **29**, 1902653.
29 Q. Yang, Q. Li, Z. Liu, D. Wang, Y. Guo, X. Li, Y. Tang, H. Li, B. Dong and C. Zhi, *Adv. Mater.*, 2020, **32**, 2001854.
30 W. Yuan, X. Nie, G. Ma, M. Liu, Y. Wang, S. Shen and N. Zhang, *Angew. Chem., Int. Ed.*, 2023, **62**, e202218386.
31 S. D. Pu, C. Gong, Y. T. Tang, Z. Ning, J. Liu, S. Zhang, Y. Yuan, D. Melvin, S. Yang, L. Pi, J. J. Marie, B. Hu, M. Jenkins, Z. Li, B. Liu, S. C. E. Tsang, T. J. Marrow, R. C. Reed, X. Gao, P. G. Bruce and A. W. Robertson, *Adv. Mater.*, 2022, **34**, 2202552.

32 J. Wang, B. Zhang, Z. Cai, R. Zhan, W. Wang, L. Fu, M. Wan, R. Xiao, Y. Ou, L. Wang, J. Jiang, Z. W. Seh, H. Li and Y. Sun, *Sci. Bull.*, 2022, **67**, 716–724.
33 D. Yuan, J. Zhao, H. Ren, Y. Chen, R. Chua, E. T. J. Jie, Y. Cai, E. Edison, W. Manalastas Jr, M. W. Wong and M. Srinivasan, *Angew. Chem., Int. Ed.*, 2021, **60**, 7213–7219.
34 M. Zhou, S. Guo, J. Li, X. Luo, Z. Liu, T. Zhang, X. Cao, M. Long, B. Lu, A. Pan, G. Fang, J. Zhou and S. Liang, *Adv. Mater.*, 2021, **33**, 2100187.
35 Z. Huang, Z. Li, Y. Wang, J. Cong, X. Wu, X. Song, Y. Ma, H. Xiang and Y. Huang, *ACS Energy Lett.*, 2023, **8**, 372–380.
36 H. Zhang, X. Gan, Z. Song and J. Zhou, *Angew. Chem., Int. Ed.*, 2023, **62**, e202217833.
37 L. Zhang, J. Huang, H. Guo, L. Ge, Z. Tian, M. Zhang, J. Wang, G. He, T. Liu, J. Hofkens, D. J. L. Brett and F. Lai, *Adv. Energy Mater.*, 2023, **13**, 2203790.
38 C. Li, R. Kingsbury, L. Zhou, A. Shyamsunder, K. A. Persson and L. F. Nazar, *ACS Energy Lett.*, 2022, **7**, 533–540.
39 D. Li, L. Cao, T. Deng, S. Liu and C. Wang, *Angew. Chem., Int. Ed.*, 2021, **60**, 13035–13041.
40 Q. Li, Y. Wang, F. Mo, D. Wang, G. Liang, Y. Zhao, Q. Yang, Z. Huang and C. Zhi, *Adv. Energy Mater.*, 2021, **11**, 2003931.
41 H. Tian, G. Feng, Q. Wang, Z. Li, W. Zhang, M. Lucero, Z. Feng, Z.-L. Wang, Y. Zhang, C. Zhen, M. Gu, X. Shan and Y. Yang, *Nat. Commun.*, 2022, **13**, 7922.
42 X. Huo, L. Xu, K. Xie, K. Zhang, J. Li, D. Wang and K. Shu, *Adv. Energy Mater.*, 2023, **13**, 2203066.
43 Z. Hu, F. Zhang, Y. Zhao, H. Wang, Y. Huang, F. Wu, R. Chen and L. Li, *Adv. Mater.*, 2022, **34**, 2203104.
44 P. X. Sun, Z. Cao, Y. X. Zeng, W. W. Xie, N. W. Li, D. Luan, S. Yang, L. Yu and X. W. Lou, *Angew. Chem., Int. Ed.*, 2022, **61**, e202115649.
45 J. Hao, B. Li, X. Li, X. Zeng, S. Zhang, F. Yang, S. Liu, D. Li, C. Wu and Z. Guo, *Adv. Mater.*, 2020, **32**, 2003021.
46 L. Yan, Y. Zhang, Z. Ni, Y. Zhang, J. Xu, T. Kong, J. Huang, W. Li, J. Ma and Y. Wang, *J. Am. Chem. Soc.*, 2021, **143**, 15369–15377.
47 K. Zhu, C. Guo, W. Gong, Q. Xiao, Y. Yao, K. Davey, Q. Wang, J. Mao, P. Xue and Z. Guo, *Energy Environ. Sci.*, 2023, **16**, 3612–3622.
48 X. Liu, F. Yang, W. Xu, Y. Zeng, J. He and X. Lu, *Adv. Sci.*, 2020, **7**, 2002173.
49 Y. Zeng, Z. Lai, Y. Han, H. Zhang, S. Xie and X. Lu, *Adv. Mater.*, 2018, **30**, 1802396.
50 R. Chen, Q. Liu, L. Xu, X. Zuo, F. Liu, J. Zhang, X. Zhou and L. Mai, *ACS Energy Lett.*, 2022, **7**, 1719–1727.
51 R. Kim, S. Yuk, J.-H. Lee, C. Choi, S. Kim, J. Heo and H.-T. Kim, *J. Membr. Sci.*, 2018, **564**, 852–858.
52 Y. Lin, Z. Mai, H. Liang, Y. Li, G. Yang and C. Wang, *Energy Environ. Sci.*, 2023, **16**, 687–697.
53 R. Chen, C. Zhang, J. Li, Z. Du, F. Guo, W. Zhang, Y. Dai, W. Zong, X. Gao, J. Zhu, Y. Zhao, X. Wang and G. He, *Energy Environ. Sci.*, 2023, **16**, 2540–2549.
54 C. Li, R. Kingsbury, A. S. Thind, A. Shyamsunder, T. T. Fister, R. F. Klie, K. A. Persson and L. F. Nazar, *Nat. Commun.*, 2023, **14**, 3067.
55 Y. Wang, B. Liang, J. Zhu, G. Li, Q. Li, R. Ye, J. Fan and C. Zhi, *Angew. Chem., Int. Ed.*, 2023, **62**, e202302583.
56 S. Carli, M. Bianchi, E. Zucchini, M. Di Lauro, M. Prato, M. Murgia, L. Fadiga and F. Biscarini, *Adv. Healthc. Mater.*, 2019, **8**, 1900765.
57 H. Ao, W. Zhu, M. Liu, W. Zhang, Z. Hou, X. Wu, Y. Zhu and Y. Qian, *Small Methods*, 2021, **5**, 2100418.
58 W. Guo, W. Zhang, Y. Si, D. Wang, Y. Fu and A. Manthiram, *Nat. Commun.*, 2021, **12**, 3031.
59 S. Liu, J. Vongsvivut, Y. Wang, R. Zhang, F. Yang, S. Zhang, K. Davey, J. Mao and Z. Guo, *Angew. Chem., Int. Ed.*, 2023, **62**, e202215600.
60 J. G. Highfield, M. H. Chen, P. T. Nguyen and Z. Chen, *Energy Environ. Sci.*, 2009, **2**, 991–1002.
61 G. N. Nomikos, P. Panagiotopoulou, D. I. Kondarides and X. E. Verykios, *Appl. Catal. B: Environ.*, 2014, **146**, 249–257.
62 C. Li, K. Domen, K. i. Maruya and T. Onishi, *J. Catal.*, 1990, **125**, 445–455.
63 J. Hao, L. Yuan, Y. Zhu, M. Jaroniec and S. Z. Qiao, *Adv. Mater.*, 2022, **34**, 2206963.
64 F. Hui and M. Lanza, *Nat. Electron.*, 2019, **2**, 221–229.
65 Y. Wang, S. A. Skaanvik, X. Xiong, S. Wang and M. Dong, *Matter*, 2021, **4**, 3483–3514.
66 P. Shi, J. Ma, M. Liu, S. Guo, Y. Huang, S. Wang, L. Zhang, L. Chen, K. Yang, X. Liu, Y. Li, X. An, D. Zhang, X. Cheng, Q. Li, W. Lv, G. Zhong, Y.-B. He and F. Kang, *Nat. Nanotechnol.*, 2023, **18**, 602–610.
67 D. Wang, D. Lv, H. Liu, S. Zhang, C. Wang, C. Wang, J. Yang and Y. Qian, *Angew. Chem., Int. Ed.*, 2022, **61**, e202212839.
68 M. H. Chung, *Electrochim. Acta*, 2000, **45**, 3959–3972.
69 B. D. Adams, J. Zheng, X. Ren, W. Xu and J. G. Zhang, *Adv. Energy Mater.*, 2018, **8**, 1702097.